Determining flame temperature by broadband two color pyrometry in a flame spreading over a thin solid in microgravity

Maria Thomsen[a,*], Juan Jose Cruz[b], Felipe Escudero[b], Andres Fuentes[b], Carlos Fernandez-Pello[c], Michael Gollner[c], David L. Urban[d], Gary A. Ruff[d]

[a] *Faculty of Engineering and Sciences, Universidad Adolfo Ibáñez, Santiago, Chile*
[b] *Departamento de Industrias, Universidad Técnica Federico Santa María, Av. España 1680, Valparaíso, Chile*
[c] *Department of Mechanical Engineering, University of California Berkeley, Berkeley, CA, USA*
[d] *NASA Glenn Research Center, 21000 Brookpark Rd., Cleveland, OH, USA*

Abstract

Fire spread inside a spacecraft is a constant concern in space travel. Understanding how the fire grows and spreads, and how it can potentially be extinguished is critical for planning future missions. The conditions inside a spacecraft can greatly vary from those encountered on earth, including microgravity, low velocity flows, reduced ambient pressure and high oxygen, and thus affecting the combustion processes. In microgravity, the contributions of thermal radiation from gaseous species and soot can play a critical role in the spread of a flame and the problem has not been fully understood yet. The overall objective of this work is to address this by studying the soot temperature of microgravity flames spreading over a thin solid in microgravity. The experiments presented here were performed as part of the NASA project Saffire IV, conducted in orbit on board the Cygnus resupply vehicle before it re-entered the Earth's atmosphere. The fuel considered is a thin fabric made of cotton and fiberglass (Sibal) exposed to a forced flow of 20 cm/s in a concurrent flow configuration. Reconstruction of the flame temperature fields is extracted from two color broadband emission pyrometry (B2CP) as the flame propagates over the solid fuel. A methodology, relevant assumptions and its applicability to other microgravity experiments are discussed here. The data obtained shows that the technique provides an acceptable average temperature around $\sim$ 1300 K, which remains relatively constant during the spread with an error value smaller than 117 K. The data presented in this work provides a methodology that could be applied to other microgravity experiments to be performed by NASA. It is expected that the results will provide insight for what is to be expected in different conditions relevant for fire safety in future space facilities.

Keywords: Broadband pyrometry; Soot temperature; Boundary layer diffusion flame; Concurrent flame spread; Sibal material.

Corresponding author: * maria.thomsen@uai.cl

1. Introduction

Understanding the behavior, spread and growth of a fire inside a spacecraft is essential to develop methods to prevent and respond to the occurrence of fire accidents that could endanger the success of a mission and the safety of the crew. Currently, materials used inside spacecraft cabins or the International Space Station (ISS) are rigorously screened to characterize their fire hazard and determine how they would behave in case of a fire [1, 2]. Although ideally, the testing of materials would be done under the actual conditions of the cabin where it is intended to be used, this is sometimes challenging given that testing in a space-based facility is very expensive and very limited in available space and opportunities.

Aiming to expand the knowledge of fire spread and growth, and material flammability in spacecraft environments, NASA embarked on a research project, the Spacecraft Fire Experiment (Saffire) [3], that aims to better understand material flammability and fire growth and spread. The Saffire experiments are a series of unique and novel large-scale spacecraft experiments performed on board the Cygnus cargo spacecraft, after the vehicle has completed its primary mission to the ISS, and before its planned destructive reentry through Earth's atmosphere. Using this vehicle to perform large-scale fire experiments was an innovative way to use a microgravity facility and alleviated the concern of crew safety for a large fire experiment. The Saffire experiments have been discussed and documented previously, and the reader is referred to Refs. [3–5] for further details. The results of the tests performed have shown that spacecraft fires could grow significantly, release enough heat and toxic gases, and persist long enough to be of concern to the crew and the spacecraft.

Despite efforts to better understand fire spread mechanisms in microgravity environments, the problem is still poorly understood [6]. Traditionally, flame spread over solid fuels has been studied in microgravity by means of tracking the flame or the pyrolysis front, providing useful but limited information of the process. As the flame spreads over the solid fuel, it acts both as the source of heat needed to pyrolyze the virgin fuel and as a pilot that later ignites the flammable mixture formed after the pyrolyzates mix with the oxidizer (see Fig. 1). Knowledge of the radiative properties of flames, in particular the temperature, are important to better understand the general process, particularly near extinction [7, 8]. Here, color pyrometry provides a useful method to determine the temperature of the flame without disruptions to the spread process. Previous studies have taken advantage of these techniques when studying diffusion flames on gas burners [9–12], however only recently the technique has been applied to spreading flames [13–15].

The results obtained during the Saffire IV experiments are revisited here to provide further information about the characterization of the flames observed during this unique experiment. Raw images obtained during the tests are analyzed to determine the temperature of the flame using broadband two color pyrometry (B2CP). It is expected that the results of this work will provide further insight into unique data obtained during microgravity experiments. Furthermore, this methodology could complement point measurements traditionally performed, providing a more complete view of the flame temperature to be used for the validation of numerical models in microgravity, and thus shedding light onto the additional processes that might play a dominant role in the spread of the flame.

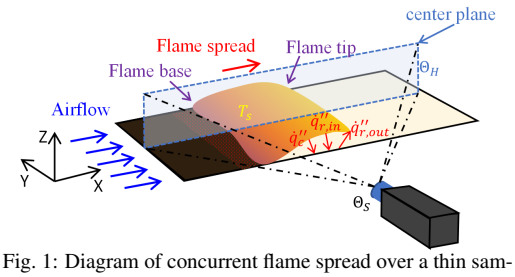

Fig. 1: Diagram of concurrent flame spread over a thin sample. Only half of the flame is schematized (symmetry is assumed with respect to the sample center plane).

2. Experimental setup

The data presented here correspond to experimental data obtained as part of the Saffire IV experiments [5] performed by NASA on board the resupply vehicle Cygnus CRS-15 before its destructive re-entry through Earth's atmosphere. A brief description about the experimental setup and procedure is given here. For further information, the reader is referred to Refs. [3, 5]. The hardware, shown in Fig. 2, was a rectangular flow duct measuring 15 cm (perpendicular to the sample surface) by 45 cm width and 109 cm length. The duct was equipped with a fan at the inlet section to induce the flow of air through the flow duct, a vane anemometer at the entrance of the inlet duct was used to monitor the flow velocity. The inlet and outlet of the duct was equipped with flow straighteners that connected to a plenum parallel to the flow duct, resulting in a folded geometry. This geometry favored flow mixing and enabled oxygen, carbon dioxide, and carbon monoxide concentration measurements at the inlet and outlet sections. In addition to the Saffire instrumentation, the vehicle was also provided with a Far Field Diagnostics unit containing a smoke cleanup system and smoke sensors.

The samples tested were placed in a holder located in the middle of the flow duct so that air flows on both sides of the sample. As part of Saffire IV, four separate fuel samples consisting of different materials and sizes were used. One of them was a custom-made combustible material, called 'Sibal fabric', which is a thin composite material made of 75% cotton and 25% fiberglass with an area density of 18.05 mg/cm^2,

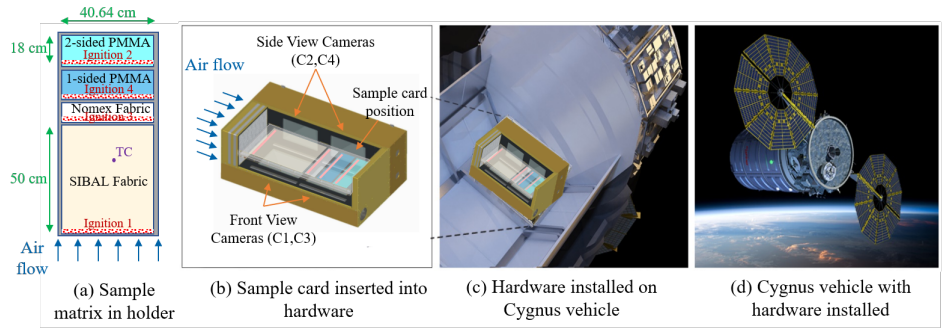

(a) Sample matrix in holder

(b) Sample card inserted into hardware

(c) Hardware installed on Cygnus vehicle

(d) Cygnus vehicle with hardware installed

Fig. 2: Schematic of the Cygnus vehicle (d), experimental setup (b, c) and sample (a).

and is the subject of this study. This material was selected both for comparison with previous microgravity tests and because the presence of the non-combustible matrix of fiberglass provides structural integrity and prevents the fabric from cracking and curling while burning, as such behavior would destroy the symmetry of the flame and complicate the flame spread process. The sample was 40.64 cm wide by 50 cm long and was mounted on a metal frame in the center of the flow tunnel (see Fig. 2). To study concurrent flame spread, a resistively-heated 29-gage Kanthal-wire (0.286 mm) was threaded through the upstream end of the sample across the entire width. The hot-wire igniter was powered for 8 s (3.98 A, 205 W) to ensure ignition of the fuel. The Sibal sample was burned in a concurrent configuration under a 20 cm/s flow velocity in an atmosphere of 22% by vol. oxygen concentration and 100 kPa ambient pressure.

Four cameras (Allied Vision Manta G 235c) were used to record images of the burning samples at 30 fps. Cameras included an IRC Hoya C-5000 IR cut filter. Two front view cameras (C1 and C3) were positioned on one side of the duct parallel to the sample to observe the full development of the flame over the material. Two side view cameras (C2 and C4) were positioned on a side of the duct, perpendicular to the sample, to observe the profiles of the flame. Cameras were configured as orthogonal pairs to image the totality of the sample holder; however, for the purpose of the present work only C1 and C2 are relevant (see Fig. 2(b)). Front and side view cameras were equipped with 6 mm (Kowa LM6HC) and 8 mm (Kowa LM8HC) lenses, respectively, to improve visualization of the flame. The flow duct was kept dark to improve flame imaging. However, the front of the fuel sample was periodically (for 0.1 s every 2 s) illuminated with four green LED strip assemblies embedded in the duct wall so that the pyrolysis front could be seen as the material burned. Four radiometers on the same side as the cameras measured radiation coming from the flame and fuel. 11 type-R thermocouples (130 μm wire diameter) were arrayed to provide temperature measurements at key locations on and near the entire fuel sample card tested, with only 4 of them placed on the Sibal fabric. Furthermore, of those four thermocouples, two were placed in direct contact with the surface to measure surface temperature, one of them malfunction during the test, and the remaining one was devoted to measure gas phase temperature. This last thermocouple was particularly relevant to the present work, and provided the means for comparison and validation purposes of technique presented here. The exact position of the device was 34 cm downstream the leading edge of the Sibal sample, 1 cm from the center line and 1 cm vertically away from the sample surface to probe the temperature of the plume.

3. Methodology

3.1. Theoretical model

The basis of the color pyrometry technique is briefly described here. The methodology presented in this work allows the measurement of the soot temperature using a conventional color camera (CMOS), employing a similar technique as developed by Jenkins and Hanson [16]. In this approach, the flame emission is simultaneously captured at three broad spectral bands to then apply pyrometry analysis. Nevertheless, is should be noted that the methodology presented in Ref. [16] uses a pulsed laser to sequentially measure the soot concentration (laser extinction) and soot temperature (flame emission). In this case, during the SAFFIRE campaign only flame emission measurements were carried out. Thus a variation of the technique had to be considered.

When imaging flames in spectral regions in which the emission is dominated by soot, the measured signal intensity represents the soot emission integrated along the line-of-sight. However, the intensity of light reaching the photo-detector can be attenuated due to the absorption and scattering of adjacent soot particles. Considering that the soot particle size is small enough to be within the Rayleigh regime, scattering effects can be neglected when compared with the effect of absorption [17]. Thus, the soot emission along a line-of-sight l across the flame, at a wavelength λ, may be described by the radiative transfer equation (RTE) [18]

$$\frac{dI_\lambda}{dl} + \kappa_\lambda I_\lambda = J_\lambda(l) \tag{1}$$

where $J_\lambda(l) = \kappa_\lambda I_\lambda^{bb}$ represents the emission of the flame. κ_λ is the soot absorption coefficient and I_λ^{bb} is

the blackbody radiative intensity defined by Planck's law at the soot temperature T_s, which in turn is assumed to be in local thermal equilibrium with the gas-phase. The solution of the radiative transfer equation along the line-of-sight of the photo-detector l allows the definition of the flame radiative intensity emitted and self-absorbed by soot particles for a given wavelength, I_λ, and can be expressed as:

$$I_\lambda(l, T_s) = \int_l \kappa_\lambda(l) I_\lambda^{bb}(T_s) \exp\left[-\int_{l'} \kappa_\lambda(l')\,\mathrm{d}l'\right]\mathrm{d}l. \quad (2)$$

Assuming that the soot particles generated by the combustion process are small enough to be within the Rayleigh regime, the soot absorption coefficient can be related to the local soot volume fraction f_v and the soot absorption function E_m through $\kappa_\lambda = f_v 6\pi E_m/\lambda$ [17]. Here, the model of Chang and Charalampopoulos [19] is considered for the soot absorption function. The exponential term in Eq. 2 represents the self-absorption along the flame path to the photodetector. This term becomes important for flames with large optical thickness; however, it can be neglected if the flame is considered to be optically thin [20]. In the present work, the soot temperature is measured considering the flame to be optically thin, and thus the effect of the self-absorption term is ignored.

When using an RGB camera, the radiative intensity of the flame I_λ is affected by the sensitivity of the detection system (η_λ). Furthermore, the photo-detector captures an intensity that is spectrally integrated in a broadband. Thus, the intensity captured by the sensor at each color channel can be defined as

$$S_i = \int_{\lambda_i} \eta_\lambda I_\lambda(l, T_s)\mathrm{d}\lambda, \quad (3)$$

with $i \in \{\mathrm{R, G, B}\}$. Assuming that the soot volume fraction remains relatively constant along the optical path, a color pyrometry ratio can be defined as done in [13, 21],

$$\Theta_{2S} = \frac{S_i}{S_j} = \frac{\int_{\lambda_i} \eta_\lambda \frac{E_m}{\lambda} I_\lambda^{bb}(T_s)\,\mathrm{d}\lambda}{\int_{\lambda_j} \eta_\lambda \frac{E_m}{\lambda} I_\lambda^{bb}(T_s)\,\mathrm{d}\lambda}. \quad (4)$$

From Eq. 4, T_s can then be obtained by employing an iterative procedure in which experimentally obtained ratios of intensities captured (LHS) are compared with the values obtained from the theoretical model (RHS) evaluated at different T_s. Similarly, a three-color ratio can also be defined by using a modified version of Eq. 4 with $\Theta_{3S} = (S_i S_j)/(S_k^2)$ [21].

3.2. Assessment of the model assumption

A deconvolution procedure is needed to convert the line-of-sight integrated signal captured by the camera into the local properties of interest. Unfortunately, this procedure requires knowledge of the flame geometry or the distribution of local properties within the flame, which is not the case for this microgravity flame. For this reason, it is assumed that the flame properties can be represented by a mean value $\bar{H}_i$ of the local flame emission H_i defined as $S_i = \int_l H_i(l)dl$ where l is the optical path through the flame to the camera. Note that the self-absorption has been neglected. Thus, the integrated flame emission can be written as $S_i = \bar{H}_i \Delta l$ where the overbar denotes the mean along the line-of-sight. As the optical length is equal for the different broadbands, considering a mean H_i (or for constant properties along the optical path), a ratio of deconvoluted signals H_i (Θ_H) is equivalent to a ratio of integrated signals S_i (Θ_S, see Fig. 1 for reference of where the ratios are computed). This hypothesis is usually not fulfilled, but alleviates the need for knowledge of flame geometry. Therefore, its impact on the retrieved temperature is assessed on a well-known flame geometry. Although the nature and geometry of the flames compared here is different to those encountered during the μg experiments, the purpose of this section is to address the validity of the established assumptions in the presence of high temperature and high soot volume fraction gradients along the medium.

A laminar coflow ethylene-air diffusion flame was used for validating the methodology. Details of the experiments, calibration and simulations used in this section can be found elsewhere [21]. The deconvoluted values of H_i are obtained either from experimental measurements or synthetic signals of S_i at three broad spectral bands. A synthetic validation is first performed. For this purpose, simulations of the signals captured by the RGB camera channels were conducted, using simulated values of temperature and soot volume fraction from a CoFlame simulation [22] as described in detail in [21]. The line-of-sight integrated signals can then be treated to retrieve a temperature that can be compared against the reference temperature provided by the simulation, as done in Fig. 3. The retrieved temperatures using deconvolution are very similar to the reference. The differences are attributed to the neglect of self-absorption for this procedure, a hypothesis that is required for the model. This effect is not important for low optical thickness, but may cause differences around 100 K for high soot volume fraction zones [23]. The temperatures retrieved without deconvoluting the signals are shown on the second row of Fig. 3(a). These temperatures are always higher than those using deconvolution, especially in zones near the flame centerline, where the flame optical thickness is highest and the hypothesis of constant properties along the camera line-of-sight is less correct. More detailed results supporting the discussion are shown on Fig. 3(b) through four radial profiles at different heights above the burner (HABs). Although the temperature retrieved without performing the deconvolution procedure is incorrectly determined as compared to the reference, its prediction is within 100 K and results on a higher temperature,

which can be thought as a safety margin for engineering applications.

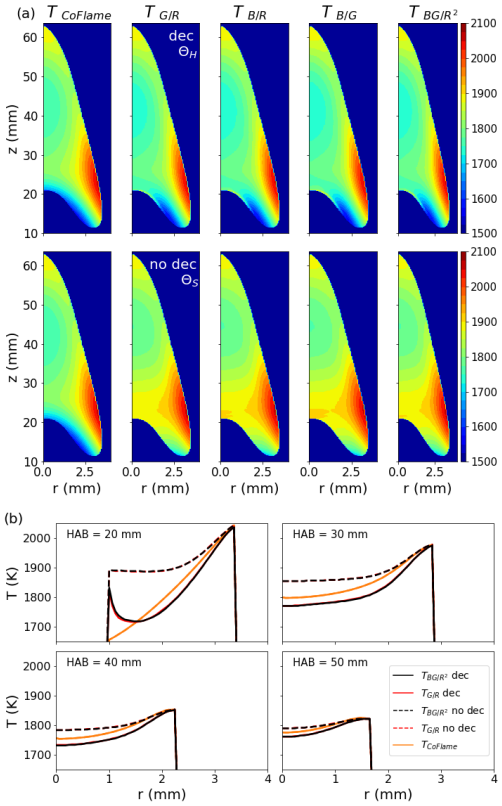

Fig. 3: (a) Temperature fields of CoFlame (first column) and retrieved using the deconvoluted ratios Θ_H (first row) and the ratios of signals captured by the camera Θ_S (second row, not deconvoluted). Colorbars denote the temperature in K. (b) Temperature profiles for the R/G and BG/R^2 signal ratios for four heights above the burner (HAB).

To complement the numerical analysis, experimental temperatures retrieved from the ratio of H_i are shown on the first row of Fig. 4(a), whereas those retrieved from the ratio of S_i are shown on the second row. The classical behavior of the deconvolution process is observed on the temperatures retrieved from local ratios of H_i, where the signal noise is propagated and enhanced toward the flame centerline. On the other hand, these issues are not observed by directly using the ratio of signals captured by the camera S_i, presenting a smooth and more uniform temperature field, at the cost of lower accuracy. Fig. 4(b) shows radial temperature profiles for four heights above the burner from 20 to 50 mm from deconvoluted (continuous) and integrated (dashed) ratios. Results are shown for the G/R and BG/R^2 channel combinations in red and black, respectively. The assumption of constant H_i within the optical path is propagated to the temperature radial profiles, which remain approximately constant until reaching a peak

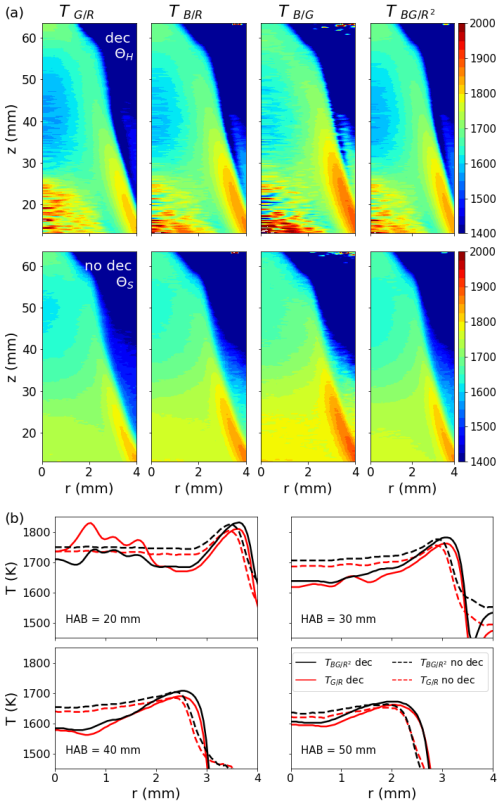

Fig. 4: (a) Experimental temperature fields retrieved using the deconvoluted ratios Θ_H (first row) and the ratios of signals captured by the camera Θ_S (second row, not deconvoluted). Colorbars denote the temperature in K. (b) Temperature profiles for the R/G and BG/R^2 signal ratios for four heights above the burner (HAB).

at the flame wings. Nevertheless, these results are within 100 K of difference with the deconvoluted results, similar to numerical results. The maximum differences are observed near the flame centerline. The peak temperature is well captured in magnitude, but it is shifted between 0.1 to 0.3 mm toward the flame centerline as compared to the reference. The best agreement is found in regions where the optical thickness is low, i.e., low soot volume fraction and flame radius, such as the flame tip. This is observed on the profiles at an HAB = 50 mm. Although there are differences between the proposed and reference approaches, these are not significant from an engineering standpoint. Therefore, this methodology allows for estimation of the mean temperature values using a commercial RGB camera.

3.3. Calibration procedure

All the cameras used in the Saffire Experiments were previously calibrated following the NIST calibration standards using equipments certified in accordance with ANSI/NCSL Z540-1-1994 [24]. The cal-

ibration of the cameras was performed using a certified blackbody source(Mikron M360) with temperatures that ranged between 973 and 1373 K. As part of this calibration procedure, images are taken in raw and bmp format under conditions of operation similar to those considered for the experiments. Simultaneously, multiple image settings are also considered. More specifically, the exposure time was varied between 60 and 29997, and the gain value was changed between 0 and 39 dB.

During the experiments, images of the flame as it spreads over the solid are recorded in RAW and JPEG formats. RAW images can then be postprocessed and converted to TIFF to proceed with the application of the broadband two color pyrometry (B2CP) technique presented above to probe temperature fields from the frames captured within visible spectrum. To ensure that no additional processing and alterations to the image are done during the conversion process, the (B2CP) technique is applied to the calibration images to verify the procedure. For this, the RHS of Eq. 4 was solved using the emissivity and temperature of the blackbody calibration source instead of the E_m/λ and T_s terms, respectively. Figure 5(a) shows a comparison between theoretical intensities ratios (S_i/S_j) presented as solid line functions and measured intensity ratios from calibration images $((S_i/S_j)_{exp})$ shown as circular symbols. From the figure it can be noted that the measured intensity ratio and the expected value at the temperature of the furnace are clearly different, suggesting that the camera adds additional processing to the files when recording them. Furthermore, the intensity of the object recorded by the sensor depends directly on the camera settings used, which during the experiments were set automatically. Thus, a correction factor is needed in order to extract appropriate values.

Given the dependence of the intensity data recorded by the sensor on the camera settings, a correction factor was determined as a function of the ratio of intensities for each color ratio considered as

$$\beta = \frac{(S_i/S_j)}{(S_i/S_j)_{exp}}. \qquad (5)$$

The correction factor functions obtained from the calibration images at know temperatures are shown in Fig. 6. It should be mentioned that, due to limitations of the equipment higher temperatures could not be tested during the calibration and thus an extrapolation of the data had to be made. The correction factor functions, β, are then used to correct the ratio of SIBAL camera images $((S_i/S_j)_{exp})$] which will then be replaced on the LHS of Eq. 4. Figure 5(a) also shows the corrected intensity ratios using the correction factor of Eq. 5. Figure 5(b,c,d,e) shows the temperature fields obtained from calibration images with the furnace at 1273 K and the correction factors calculated. It is seen that with the correction factors, the extracted temperature fields approximate very well the temperature of the furnace with the exception of the

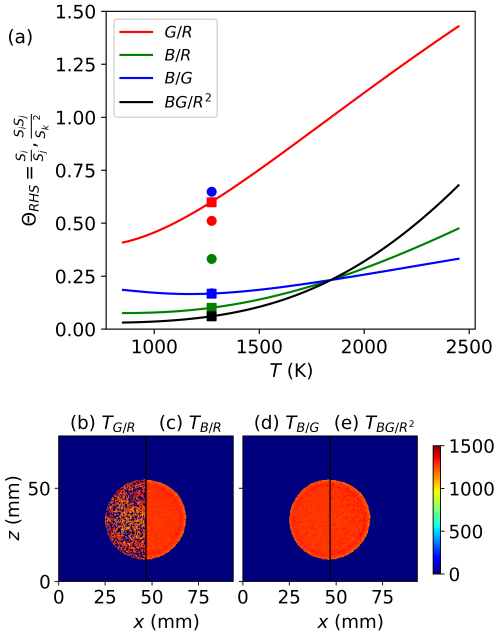

Fig. 5: (a) Comparison between theoretical (solid line functions) and measured intensity ratios with (squares) and without (circles) the correction factor. Temperature fields determined with the calibration images at $T_{furnace}$=1273K using different color ratios (b,c,d,e) and the correction factors of Eq. 5

G/R ratio. The discrepancies observed with the G/R ratio are generated because of the shape of the correction factor (β) curve that when applied to the intensity ratios (S_i/S_j) at lower temperatures generates more than one plausible solution for an intensity ratio.

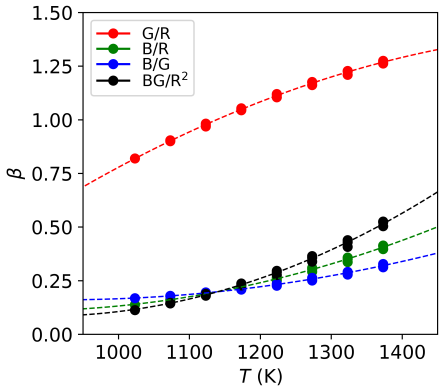

Fig. 6: Correction factor evolution as a function of temperature of the imaged object.

4. Flame temperature

During the spread process, after ignition is achieved and the igniter is turned off, the flame

spreads uniformly along the surface of the sample. As the flame spreads over the composite fabric, it consumes most of the cotton, leaving behind the fiberglass mesh and some smoldering cotton residue. During this process, periodic images are taken of the spread process. These images are later corrected for perspective issues and processed to extract soot temperature. Considering that the initial purpose of the images recorded during the experiments was to use the data to visualize the flame and track its evolution over time, i.e., pyrolysis length, flame size, etc., the cameras used in the experiments were set to automatically modify their settings to better visualize the flames. Due to this, some of the images would present high levels of saturation, particularly near the center of the flame, making it impossible to extract any relevant information in the area. Thus, when performing the color pyrometry ratios, channels green and blue were preferred for determining the temperature.

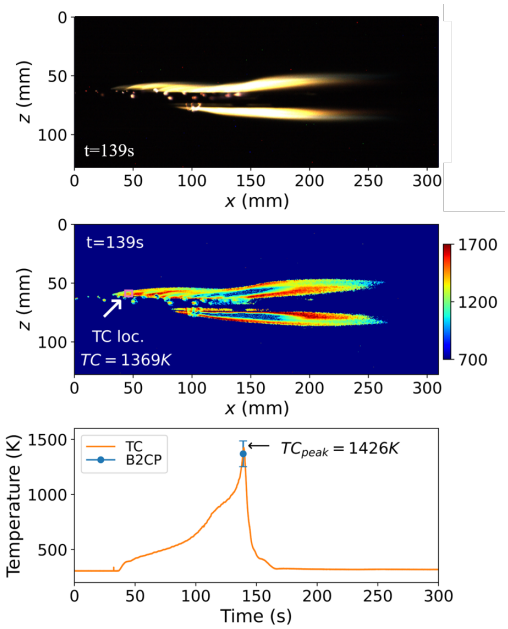

Fig. 7: Comparison between the original data [5] (top), B2CP temperature fields (center) and the temperature measurement from the thermocouple (bottom).

Figure 7 shows the temperature field of the flame as determined by the B2CP technique. This image was selected to match the instant of time that the thermocouple measuring above the surface, in the fire plume, reaches the peak recorded value (TC_{peak}), as shown in the bottom portion of Fig. 7. The thermocouple measurements have been corrected for radiation and convection effects [25]. From the figure it is seen that at the exact point of the thermocouple position, B2CP gives a temperature close to 1369 K which is relatively close to the 1426 K recorded by the device at the same instant in time. This comparison validates both the technique and the correction functions previously determined. The relative uncertainty associated with the thermocouple reading has been estimated following the work of Ren et al. [26]. A relative uncertainty for a type-R thermocouple of 0.25% is considered, thus resulting in an overall correction for radiation and convection effects of $\pm$ 6 K in the measured value. The error for B2CP technique was computed from a Monte Carlo propagation analysis, considering a conservative error of 5% on the signal ratio $\Theta_{G/R}$, resulting in 117 K of uncertainty for temperature determination. With this, both measurements are comparable within the error margin.

Figure 8 shows flame images at different selected times after the test is initiated and ignition achieved, together with the corresponding temperature fields. At first, the flame shape for the large-scale sample looks a bit distorted because the camera's field of view does not reach the entire sample holder. For the initial 120 s, the flame kept its symmetrical shape between the top and bottom part. After that, the top flame seems to be pushed closer to the surface, getting longer than the bottom flame. Towards the end of the spread, only small smoldering spots were left burning some of the unconsumed fuel. The temperature fields of Fig. 8 show that during the spread process the flame temperature does not change very significantly, staying constant at an average of 1305 K soon after ignition and throughout the entire test. Lastly, when looking at the results presented in Figs. 7 and 8, the reader should keep in mind that no temperature values could be determined near the center of the flame (the most luminous part) because the saturation level presented by the raw images made it impossible to extract any sort of useful information at those locations. Given that issue, temperature values were artificially set to 0 to be able to plot the entire flame field.

5. Concluding remarks

The present paper presents a methodology and analysis of broadband two color pyrometry technique applied to a spreading diffusion flame in microgravity conditions. The proposed model is validated using numerical simulations and experimental measurements of well-known coflow flames. The validation process supports the major assumptions of the analysis and shows that the technique provides an acceptable average temperature, although it is biased toward higher values. The processed RAW data from the recorded images results in temperature in accordance with thermocouple measurements of the plume obtained during the experiment. The information extracted from the recorded images provides additional insights of the flame characteristics observed during the Saffire IV experiments, showing that the flame temperature remains relatively constant during the entire spread process. The application of this technique in this configuration can be coupled with soot volume fraction measurements in order to estimate the radiative heat flux emitted by the flame, in order to design

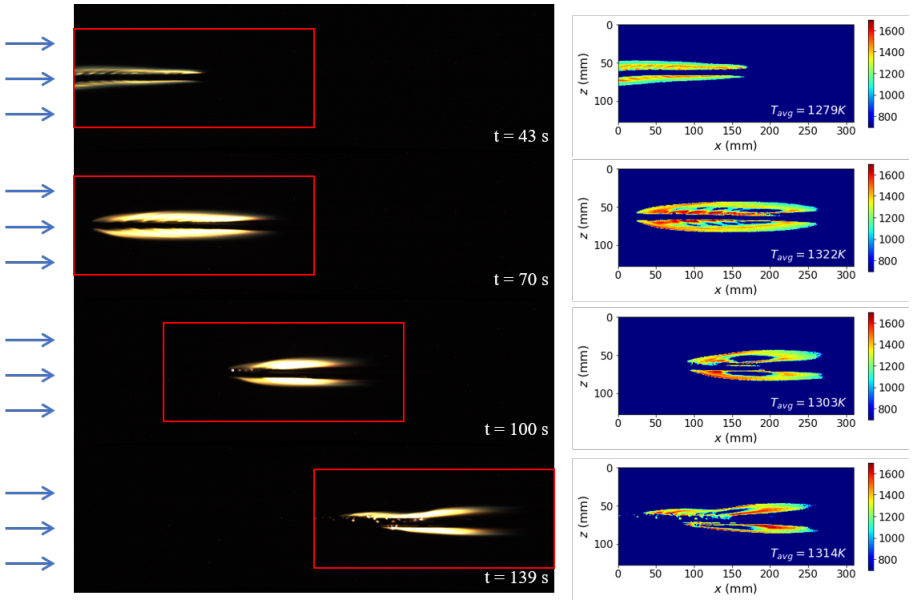

Fig. 8: A sequence of images from the spreading flame in a forced flow in microgravity conditions. Images on the left show snapshots as recorded from the camera after correcting for perspective issues [5]. Images on the right show the temperature fields obtained with the B2CP technique. All images have the same scale.

fire safety strategies for spacecraft.

Acknowledgments

The authors acknowledge the support of the NASA Advanced Exploration Systems Division for the sponsorship of the Spacecraft Fire Safety Demonstration Project and the Saffire experiments. The authors would also like to thank Grunde Jomaas, Augustin Guibaud, and Guillaume Legros for their insightful comments. Maria Thomsen would also like to thank Fondecyt 3200964.

References

[1] National Aeronautics and Space Administration, NASA-STD-6001B Flammability, Offgassing, and Compatibility Requirements and Test Procedures, Tech. Rep. I, Washington, DC (2011).

[2] ECSS Secretariat, ECSS-Q-ST-70-21C Space product assurance - Flammability testing for the screening of space materials, Tech. Rep. February (2010).

[3] D. L. Urban, P. Ferkul, S. Olson, G. A. Ruff, J. S. T'ien, Y.-t. T. Liao, A. C. Fernandez-Pello, J. L. Torero, G. Legros, C. Eigenbrod, N. Smirnov, O. Fujita, S. Rouvreau, B. Toth, G. Jomaas, Flame Spread : Effects of Microgravity and Scale, Combustion and Flame 199 (2019) 168–182.

[4] G. Jomaas, J. L. Torero, C. Eigenbrod, J. Niehaus, S. L. Olson, P. V. Ferkul, G. Legros, A. C. Fernandez-Pello, A. J. Cowlard, S. Rouvreau, N. Smirnov, O. Fujita, J. S. T 'ien, G. A. Ruff, D. L. Urban, Fire safety in space – beyond flammability testing of small samples, Acta Astronautica 109 (2015) 208–216.

[5] D. L. Urban, G. A. Ruff, P. Ferkul, J. Easton, J. Owens, S. Olson, M. Meyer, C. Fontenberry, J. E. Brooker, J. Graf, M. Casteel, B. Toth, F. Meyer, C. Eigenbrod, J. S. Tien, Y.-t. T. Liao, C. Fernandez-pello, G. Legros, A. Guibaud, N. Smirnov, O. Fujita, G. Jomaas, Fire Safety Implications of Preliminary Results from Saffire IV and V Experiments on Large Scale Spacecraft Fires, in: 50th International Conference on Environmental Systems, 2021.

[6] G. A. Ruff, Microgravity Research in Spacecraft Fire Safety, Halon Options Technical Working Conference (April) (2001) 13–22.

[7] H. D. Ross, Basics of Microgravity Combustion, in: H. D. Ross (Ed.), Microgravity Combustion: Fire in Free Fall, 2001, Ch. 1, pp. 1–33.

[8] S. Takahashi, M. Kondou, K. Wakai, S. Bhattacharjee, Effect of radiation loss on flame spread over a thin PMMA sheet in microgravity, Proceedings of the Combustion Institute 29 (2002) 2579–2586.

[9] J. Reimann, S. Will, Optical diagnostics on sooting laminar diffusion flames in microgravity, Microgravity Science and Technology 16 (1) (2005) 333–337.

[10] J. Reimann, S. A. Kuhlmann, S. Will, Investigations on soot formation in heptane jet diffusion flames by optical techniques, Microgravity Science and Technology 22 (4) (2010) 499–505.

[11] K. J. Santa, B. H. Chao, P. B. Sunderland, D. L. Urban, D. P. Stocker, R. L. Axelbaum, Radiative extinction of gaseous spherical diffusion flames in microgravity, Combustion and Flame 151 (4) (2007) 665–675.

[12] M. Zhu, H. Zhang, G. Tang, Q. Liu, J. Lu, G. Yue, S. Wang, S. Wan, Ignition of single coal particle in a hot furnace under normal- And micro-gravity condition, Proceedings of the Combustion Institute 32 II (2) (2009) 2029–2035.

[13] A. Guibaud, J. L. Consalvi, J. M. Orlac'h, J. M. Citerne, G. Legros, Soot Production and Radiative Heat Transfer in Opposed Flame Spread over a Polyethylene Insulated Wire in Microgravity, Fire Technology (2019).

[14] A. Guibaud, J. M. Citerne, J. M. Orlac'H, O. Fujita, J. L. Consalvi, J. L. Torero, G. Legros, Broadband modulated absorption/emission technique to probe

sooting flames: Implementation, validation, and limitations, Proceedings of the Combustion Institute 37 (3) (2019) 3959–3966.

[15] A. Guibaud, J. M. Citerne, J. L. Consalvi, J. L. Torero, O. Fujita, M. Kikuchi, P. V. Ferkul, N. Smirnov, G. Jomaas, B. Toth, S. Rouvreau, G. Legros, Accessing the soot-related radiative heat feedback in a flame spreading in microgravity: Optical designs and associated limitations, in: Proceedings of the Combustion Institute, Vol. 38, Elsevier Ltd, 2021, pp. 4805–4814.

[16] T. P. Jenkins, R. K. Hanson, Soot pyrometry using modulated absorption/emission, Combustion and Flame 126 (3) (2001) 1669–1679.

[17] M. Modest, Radiative Heat Transfer, Academic Press, 2013.

[18] R. Viskanta, M. P. Mengüç, Radiation heat transfer in combustion systems, Progress in Energy and Combustion Science 13 (2) (1987) 97–160.

[19] H. Chang, T. T. Charalampopoulos, Determination of the Wavelength Dependence of Refractive Indices of Flame Soot, Proceedings of the Royal Society A: Mathematical, Physical and Engineering Sciences 430 (1880) (1990) 577–591.

[20] F. Liu, K. A. Thomson, G. J. Smallwood, Soot temperature and volume fraction retrieval from spectrally resolved flame emission measurement in laminar axisymmetric coflow diffusion flames: Effect of self-absorption, Combustion and Flame 160 (9) (2013) 1693–1705.

[21] J. J. Cruz, F. Escudero, E. Álvarez, L. F. Figueira da Silva, G. Carvajal, M. Thomsen, A. Fuentes, Three-wavelength broadband soot pyrometry technique for axisymmetric flames, Optics Letters 46 (11) (2021) 2654.

[22] N. A. Eaves, Q. Zhang, F. Liu, H. Guo, S. B. Dworkin, M. J. Thomson, Coflame: A refined and validated numerical algorithm for modeling sooting laminar coflow diffusion flames, Comput. Phys. Commun. 207 (2016) 464–477.

[23] J. J. Cruz, L. F. F. da Silva, F. Escudero, F. Cepeda, J. C. Elicer-Cortés, A. Fuentes, Soot pyrometry by emission measurements at different wavelengths in laminar axisymmetric flames, Combustion Science and Technology 194 (8) (2022) 1643–1660.

[24] American National Standard for Calibration, Calibration laboratories and measuring and test equipment - General requirements, Tech. rep. (1994).

[25] C. R. Shaddix, Correcting Thermocouple Measurements for Radiation Loss: A Critical Review, in: Proceedings of the 33rd National Heat Transfer Conference, Albuquerque, New Mexico, 1999, pp. 1–10.

[26] X. Ren, D. Zeng, Y. Wang, G. Xiong, G. Agarwal, M. Gollner, Temperature measurement of a turbulent buoyant ethylene diffusion flame using a dual-thermocouple technique, Fire Safety Journal 120 (January) (2021) 103061.